Sea Trial on Deterministic Sea Waves Prediction Using Wave-Profiling Radar

Mustafa Al-Ani*, Michael Belmont, and Jacqueline Christmas

College of Engineering, Mathematics and Physical Sciences, University of Exeter, Exeter, UK.

* Corresponding author. E-mail address: m.t.a.al-ani@exeter.ac.uk

ABSTRACT

Short-term deterministic sea wave prediction (DSWP) can facilitate the safe implementation of a number of maritime operations. Wave profile radars, based on the conventional X-band radars, have recently been proven to provide a low-cost convenient source of two-dimensional wave measurement for DSWP. The Golden Arrow sea trial in the North Atlantic was dedicated to collecting wave and vessel motion data for DSWP purposes, particularly under the large sea conditions that are of practical interest in marine operations. The field data were collected using a wave profiling radar and other measurement technologies for validation. This paper reports on the successful application of a recently developed technique by Al-Ani et al. in DSWP to the dedicated sea trial.

Keywords - Deterministic sea wave prediction (DSWP); quiescent period prediction (QPP); sea trial; wave profiling radar

1. Introduction

Short-term deterministic sea wave prediction (DSWP) can potentially play a useful role in extending the sea states under which many critical maritime operations can be safely undertaken (Crossland et al., 2009; Giron-Sierra and Esteban, 2010; Ferrier et al., 2013). DSWP as a branch of marine science had its roots in the early 1990’s and has recently evolved into a rapidly growing discipline, an illustrative sample of the literature being Morris et al. (1992), Pourzanjani et al. (1992), Blondel et al. (2008), Belmont et al. (2014), Hilmer and Thrinhill (2014), and Connell et al. (2015). Unlike traditional statistical estimation of sea wave properties (Tucker and Pitt, 2001), the discipline of DSWP aims to predict (few tens of seconds in advance) the actual profile of the sea surface and its evolution. Typical prediction timescales are in the range of 60-120 s ahead. Two common elements make DSWP an attractive tool in safely operating many launch and recovery tasks including: the launch and recovery of fixed and rotary wing aircraft; small, surface or submersible vehicles, such as RHIBs; and cargo, fuel, and personnel transfer systems between vessels, and vessels onto offshore structures. Firstly, while the overall execution of such tasks may take a significant amount of time, the key wave-height-critical sub-tasks that actually limit the sea state under which they can be carried out are short, typically less than one minute. Secondly, a fundamental property of most sea conditions encountered that are of relevance to ships is that sets of large waves alternate with sets of smaller waves, the exception being highly multidirectional large wind-wave seas encountered within very strong storm systems when the wind conditions themselves typically prohibit most launch and recovery operations. The smaller waves present in otherwise large seas are, by definition, of lower height than the standard sea statistics for the prevailing conditions, and consequently the intervals in which these lower height waves occur are referred to as *quiescent periods*. Combining the above two elements, i.e. the relatively short duration of the wave-height critical sub-tasks and the presence of quiescent periods, suggests that if the smaller waves could be deterministically predicted then a range of maritime operations could be safely undertaken under conditions whose overall sea state statistics would prohibit the execution of the task. Hence, there is an increasing interest in the capabilities, such as quiescent period prediction (QPP), that are based upon DSWP (Pourzanjani et al., 1992; Ferrier et al., 2000; Crossland et al., 2009; Ferrier et al., 2013).

As discussed in Belmont et al. (2014), wave profiling radars are the only realistic sensing technology for shipborne applications of DSWP. Conventional vessel-mounted wave radar returns statistical wave data (sea surface roughness). In contrast, the OceanWaveS WaMoS II wave profiling radar (Reichert et al., 1999) offers the prospect of measuring the actual sea surface profile over an area of a few square kilometres around a vessel, based on the standard X-band radar carried by ships for safe navigation purposes. In Hilmer and Thornhill (2014), the accuracy of WaMoS II at rendering sea surface elevation was evaluated against a wave buoy, where the majority of correlation coefficients exceeded 0.87. Due to the commercial nature of the source, full details of all the processing algorithms employed in extracting wave profiles from radar backscatter data are not available to users and their details are understandably not fully disclosed in the company's published material (Hilmer and Thornhill 2015).

Using experimental wave profiling radar, Belmont et al. (2014) explored two forms of DSWP techniques. The first was so called "multiple fixed point" system based upon setting up a system of equations that described a sea composed of a modest number of wave directions. This approach had some success. Secondly a fully two-dimensional method in the form classic discrete time Fourier transform was employed that was slightly less effective. The WaMoS II system was deployed during a sea trial, designated as Golden Arrow, undertaken expressly to gather data for DSWP purposes. A fundamental challenge inherent in the use of WaMoS II is that it employs standard navigation radars whose antenna are typically mechanically rotated with scan times of few seconds. This means that the radar backscatter data evolves in both time and space and hence simple spatial Fourier techniques are only valid where the scan period is very small compared to the shortest period of interest. In the Golden Arrow trial, the rotational period of 2.52 s is considerable compared to the dominant wave periods of 11 s and 13 s for the prevailing westerly and south-westerly wave systems.

In order to address the above problem, a new two-dimensional approach was developed in Al-Ani et al. (2019). This technique can accept the mixed space-time data arising from the rotating radar antenna and furthermore is not susceptible to the condition number problems that usually arise with any form of inversion into prediction models (e.g., Alford et al. (2015), Belmont et al. (2014) and Connell et al. (2015)). When applied to simulated wave data, the new technique produces very promising results (Al-Ani et al., 2019). In the present report, the authors focus on applying this approach to the field data of the Golden Arrow and report on the wave prediction accuracy achieved.

The remainder of the paper is organised as follows. In Section 2, the authors summarise the key elements of the new technique. The performance metrics that are used to assess the quality of prediction are detailed in Section 3. In Section 4, we describe the sea trial data and illustrate the accuracy of the wave profiles prediction. In Section 5, conclusions are drawn.

2. DSWP Technique

The prediction model is based on the standard linear oceanographic wave model of the sea surface elevation $h(x, y, t)$ at the spatial coordinate (x, y), and temporal coordinate t that is given by

$$h(x,y,t) = \sum_{r=1}^{R}\sum_{n=1}^{N}[\, a_{n,r}\cos(k_n x\cos(\theta_r) + k_n y\sin(\theta_r) - \omega_n t)$$

$$+b_{n,r}\sin(k_n x\cos(\theta_r) + k_n y\sin(\theta_r) - \omega_n t)], \qquad (1)$$

where N is the number of spectral components in the propagation direction θ_r, R is the number of directions, $(a_{n,r}, b_{n,r})$ is the spectral coefficient pair at the wavenumber k_n and its angular frequency ω_n in the direction θ_r. With this technique, use is made of the standard oceanographic assumption (Tucker et al., 1984) that in the Fourier transform of a particular set of wave profile data the spectral coefficients are considered to be statistically independent. (It is important to distinguish the spectrum of a particular set of sea data from spectral models, such as Pierson Moskowitz or JONSWAP, which represent the average of a large number of such individual spectra.)

For a more compact representation, let

$$\alpha_{n,r}(x,y,t) \triangleq \cos(k_n x\cos(\theta_r) + k_n y\sin(\theta_r) - \omega_n t)\ , \qquad (2)$$

$$\beta_{n,r}(x,y,t) \triangleq \sin(k_n x\cos(\theta_r) + k_n y\sin(\theta_r) - \omega_n t)\,. \qquad (3)$$

Furthermore, we let $z = (x, y) \in \mathbb{R}^2$. The sea elevation discrete measurements from one radar scan is denoted by $\{h_s(\mathrm{z}_m, t_{s,m})\}_{m=1}^{M}$, $\mathrm{z}_m = (x_m, y_m)$, where M is the size of the discrete data per scan s (or a subdomain of the scan used in building the prediction model). For a single scan s, the sequence $\{t_{s,m}\}_{m=1}^{M}$ range over the period $(\tau_s, \tau_s + \Delta t]$, where τ_s is the start time of the scan and Δt is the rotation time of the radar antenna, and $\{(x_m, y_m)\}_{m=1}^{M}$ range over the radar scan spatial area.

The coefficients $a_{n,r}$ and $b_{n,r}$ can be determined by solving the following minimization tasks

$$\min_{a_{n,r}, b_{n,r}} \sum_{m=1}^{M} \left[a_{n,r}\alpha_{n,r}(\mathrm{z}_m, t_{s,m}) + b_{n,r}\beta_{n,r}(\mathrm{z}_m, t_{s,m}) - h_s(\mathrm{z}_m, t_{s,m})\right]^2. \tag{4}$$

The solution is given by

$$\begin{bmatrix} \hat{a}_{n,r} \\ \hat{b}_{n,r} \end{bmatrix} = \mathbf{H}^{-1}\mathbf{f}\,, \tag{5}$$

where

$$\mathbf{H} = \sum_{m=1}^{M} \begin{bmatrix} \alpha_{n,r}(\mathrm{z}_m, t_{s,m}) \\ \beta_{n,r}(\mathrm{z}_m, t_{s,m}) \end{bmatrix} \begin{bmatrix} \alpha_{n,r}(\mathrm{z}_m, t_{s,m}) & \beta_{n,r}(\mathrm{z}_m, t_{s,m}) \end{bmatrix} \quad , \tag{6}$$

$$\mathbf{f} = \sum_{m=1}^{M} \begin{bmatrix} \alpha_{n,r}(\mathrm{z}_m, t_{s,m}) \\ \beta_{n,r}(\mathrm{z}_m, t_{s,m}) \end{bmatrix} h_s(\mathrm{z}_m, t_{s,m}) \quad . \tag{7}$$

We can see that $\mathbf{f}$ is of size 2×1, $\mathbf{H}$ is 2×2, and the solution in (5) is 2×1 which represents a single pair of spectral coefficients at wavenumber k_n in direction θ_r. The solution (5) is determined for each of the RN spectral pairs in a one-by-one manner. This technique is related to the single-frequency least-squares estimation in nonuniform sampling theory, which is also known under other names, such as the Lomb-periodogram, depending on the application (Stoica et al., 2011).

The solution in (5) requires inverting **H** - a matrix of size 2×2. This is more numerically stable than inverting potentially large $(R \times R)$ matrices involved in the Multiple Fixed Points method (Belmont et al., 2014) and even larger $(RN \times RN)$ matrices involved in the classical least-squares fitting of the data to all the spectral components *simultaneously,* which are equivalent to solving Vandermonde systems that are well-known to be poorly conditioned with condition numbers that rise with their ranks (Bagchi and Mitra, 1996; Bilinskis, 2007; Belmont et al., 2014). We can also observe that the technique accounts for the varied time instants of the measurements across the scan (unlike the standard two-dimensional Fourier transform, used for example in Wijaya et al. (2015), where a single time instant is associated with each scan).

We note that the spectral components along with their coefficients in the prediction model can represent the sea surface elevation in the measurement and predictable zone at defined temporal points. This means that the prediction model is not a general representation of the prevailing sea and the coefficients derived from different scans are in fact independent.

3. Performance Metrics

The S scans collected over the sea trial are denoted by $\hbar_s = \{h_s(\mathrm{z}_m, t_{s,m})\}_{m=1}^{M}, s = 1, \dots, S$ and used respectively to generate predictions of the sea surface over the *prediction horizon* $\mathcal{T} = (\tau_s, \tau_s + T]$, where T is the total prediction time (it is important to clarify that the term 'prediction horizon' here is used to indicate a time period as opposed to a single time instant). The prediction of the sea surface based on $\hbar_s$ at prediction time instant $t_{s+p,m} \in (\tau_s, \tau_s + T], p = 1, .., P$, where $P = T/\Delta t$, is denoted by $\{\hat{h}_s(z_m, t_{s+p,m})\}_{m=1}^{\widehat{M}}$, where $\widehat{M}$ is the size of the spatial *predictable zone*. The relationship between the available prediction horizon, predictable zone, and the properties of the measurements can be described by the so called Space-Time diagrams (Edgar et al., 2000; Abusedra and Belmont, 2011; Qi et al., 2018) which yield all the necessary information. In the multidimensional seas, the Space-Time diagrams are applied in all propagation directions with the final results being the intersection of the diagrams from all directions, see for example Qi et al. (2018) for an illustration.

The first metric for assessing the prediction accuracy is the (temporal) correlation between the predicted and true wave profiles. In maritime applications such as helicopter recovery at sea, it is more valuable from a practical point of view to evaluate the correlation in the temporal domain at a single spatial location (as opposed to the spatial correlation at a single time instant). Therefore, formally speaking, we determine the normalised correlation between the predicted wave profile for the prediction horizon $\mathcal{T} = (\tau_s, \tau_s + T]$, at a spatial location and the "future" radar data available to us within the same time horizon and location. Assuming that the predicted and true wave profiles, $\left\{\hat{h}_s\left(z_m, t_{s+p,m}\right)\right\}_{p=1}^{P}$ and $\left\{h_{s+p}\left(z_m, t_{s+p,m}\right)\right\}_{p=1}^{P}$ respectively, are zero-centred, their correlation coefficients based on $\hbar_s$ are given by

$$\mathrm{Q}_s(z_m) = \frac{\frac{1}{P}\sum_{p=1}^{P} \hat{h}_s\left(z_m, t_{s+p,m}\right) h_{s+p}\left(z_m, t_{s+p,m}\right)}{\hat{\sigma}_s(z_m)\sigma_s(z_m)}\ , \quad s = 1, \dots, S, \quad m = 1, \dots, \widehat{M} \qquad (8)$$

where

$$\hat{\sigma}_s(z_m) = \left[\frac{1}{P}\sum_{p=1}^{P}\left|\hat{h}_s\left(z_m, t_{s+p,m}\right)\right|^2\right]^{1/2}, \qquad (9)$$

$$\sigma_s(z_m) = \left[\frac{1}{P}\sum_{p=1}^{P}\left|h_{s+p}\left(z_m, t_{s+p,m}\right)\right|^2\right]^{1/2}. \qquad (10)$$

For overall illustration of the results of (8), we average the correlation coefficients at each location z_m across the scans, i.e. $A(z_m) = \frac{1}{S}\sum_{s=1}^{S}\mathrm{Q}_s(z_m)$. To further analyse the prediction accuracy within the prediction horizon, we obtain a second form of temporal correlation where we evaluate the inner product along the trial duration for a single time *instant* ($t_{s+p} \in (\tau_s, \tau_s + T]$) in the prediction horizon:

$$\mathrm{Q}_p(z_m) = \frac{\frac{1}{S}\sum_{s=1}^{S} \hat{h}_s\left(z_m, t_{s+p,m}\right) h_{s+p}\left(z_m, t_{s+p,m}\right)}{\hat{\sigma}_p(z_m)\sigma_p(z_m)}\ , \quad p = 1, \dots, P, \quad m = 1, \dots, \widehat{M} \qquad (11)$$

where

$$\hat{\sigma}_p(z_m) = \left[\frac{1}{S}\sum_{s=1}^{S}\left|\hat{h}_s(z_m, t_{s+p,m})\right|^2\right]^{1/2}, \tag{12}$$

$$\sigma_p(z_m) = \left[\frac{1}{S}\sum_{s=1}^{S}\left|h_{s+p}(z_m, t_{s+p,m})\right|^2\right]^{1/2}. \tag{13}$$

Nonetheless, the correlation coefficient demonstrates the accuracy of predicting the shape of the wave profile and not its amplitude (Taylor 2001). Therefore, as an additional performance metric, we determine the relative RMS errors

$$\mathrm{E}_{\mathbf{s}}(z_m) = \left[\frac{1}{P}\sum_{p=1}^{P}\left|\varepsilon_s^p(z_m)\right|^2\right]^{1/2}, \qquad s = 1, \dots, S, \quad m = 1, \dots, \hat{M} \tag{14}$$

where,

$$\varepsilon_s^p(z_m) = \frac{\hat{h}_s(z_m, t_{s+p,m}) - h_{s+p}(z_m, t_{s+p,m})}{H_s(z_m)} \tag{15}$$

where $H_s(z_m)$ represents the maximum wave height at location z_m in the specified prediction horizon.

4. The Sea Trial and Results

The illustrative data presented here was obtained during an interval of long-period high sea state during the Golden Arrow sea trial on the 24th November 2014 between 9:20 and 14:00 UTC off the western coast of Scotland, approximately 100 km west of the Isle of Mull. The development of the wave system during this part of the trial as reflected by the vessel's wave driven heave motion is shown in Fig. 1, where the standard deviation of the ship heave is calculated over a window of ten minutes.

Statistical directional wave spectra were determined from both: the WaMoS II wave radar (operating in traditional statistical mode as opposed to wave profiling mode) and free floating directional multi-axis wave buoys. Both data sources indicated that there were two significant wave directions, one from the west and one from the south west. (Here the wave directions represent the direction the waves are propagating from.) The dominant periods of these two wave systems were up to 11 s and 13 s, respectively. These timescales were significant as the 3dB point of the vessel frequency response in heave corresponds to 9 s period waves. Thus, to a zeroth-order approximation, the vessel acted as a wave follower in heave as will be discussed later. Between 13:00 and 14:00 UTC the ship was manoeuvring slowly and the waves were at their highest, and therefore the study is focused in this hour. The speed, course and heading of the ship from 12:58 to 14:00 UTC is shown in Fig. 2.

4.1 Wave profiles predictions

A subdomain from each WaMoS II scan is chosen, where the measurements are most reliable. The size and location of the reliable *measurement zone*, also known as the "sweet spot" in the literature, depends on the sea waves properties, radar height and characteristics, and the prediction requirements. It is usually located in the directions where waves are traveling towards the radar, beyond the dead zone around the ship where the radar backscatter is saturated, and therefore it usually follows the shape of a section of a ring (see, for example, Qi et al. (2016) for a discussion). For easy illustration, we restrict the measurement zone here to a trapezium, west of the ship. The dimensions and location of the measurement trapezium are illustrated in Fig.3 a. The axes in Fig. 3 are labelled according to the ship location that is set at the spatial location (0,0) m.

The wavenumbers $\{k_n\}_{n=1}^{N}$ in (1) are set to uniformly span over the longest and shortest waves to represent. The angular directions $\{\theta_r\}_{r=1}^{R}$ are evenly distributed over a half plane The wavenumber resolution in (1) is defined by π/γ, where γ is the radius of the scan that is 3 km here. The directional resolution depends on the choice of the maximum wavenumber k_N and is defined by $2\pi/\gamma k_N$. Given that the dominant wavenumbers for the two dominant storm systems are 0.033 rad/m, and 0.024 rad/m, it was deemed reasonable to limit the maximum wavenumber to 0.09 rad/m in (1). Thus, the number of directions R and the number of spectral components N per direction are 135 and 85, respectively. To determine all the coefficients in the prediction model (1), the presented technique requires $O(MRN)$ operations, where the number of signal samples M in the measurement zone is 150×10^3 per scan. The computations are more demanding than an FFT, which typically requires $O(M\log M)$ operations. However, an interpolation into a Cartesian grid is prerequisite in order for an FFT to be deployed, unlike the presented method that can handle data of any distribution with no extra computations. We note that increasing the number of wave components in (1) does not improve the prediction performance. Whereas, using the full resolution of the data inside the measurement zone offers an improvement in the prediction quality as the effect of measurements noise and jitter reduces with the number of data points used.

The data from the measurement zone of the s-th scan is used to build the prediction model which in turn is used to yield the sea surface motion over the corresponding predictable zone for prediction horizons $\mathcal{T}_1 = [\tau_s, \tau_s + 30]$ s, $\mathcal{T}_2 = [\tau_s, \tau_s + 60]$ s, $\mathcal{T}_3 = [\tau_s, \tau_s + 90]$ s, $\mathcal{T}_4 = [\tau_s, \tau_s + 120]$ s, $\mathcal{T}_5 = [\tau_s, \tau_s + 150]$ s. It was adequate for illustration to simply identify the predictable zones by a single boundary from the west which we set to 5 m/s. It is important to note that in the correlation and prediction error calculations, we use the radar measurements available to us as the “true and future” waves. Therefore, the errors in the latter contribute to the performance results presented here. To minimise this effect, we illustrate the prediction accuracy in the areas where the reliable measurement zone and the predictable zones overlap. In Fig. 3. b – f, we show the mean correlation coefficients $A(z_m)$ in these overlapping areas. We can see that $A(z_m)$ vary around 0.95 for $\mathcal{T}_1$, and mainly around 0.92 for $\mathcal{T}_2$, i.e. one minute ahead. For $\mathcal{T}_3$, we can see $A(z_m)$ to range between 0.85 and 0.95. The mean correlation coefficients are around 0.85 for $\mathcal{T}_4$, i.e. two minutes ahead. Finally, the mean correlation coefficients go mostly down around 0.8 for $\mathcal{T}_5$. We can observe that the correlation degrades with increasing the time horizon even with the conservative predictable zones set here, which is somehow expected. However, the high values of correlations are evident in the plots especially for time horizons shorter than two minutes. To show the reliability of prediction across the hour, we include Fig. 4 which represents box plots that illustrate the distributions of the correlation coefficients. We can observe that the correlation degrades at 1– 3 min, 18 min, 25 – 37 min, and 47-50 min past 13:00 UTC. These times can, to an extent, be linked to times when the ship had been changing its speed in Fig. 2. A possible explanation is that the change in speed, heading and course can introduce measurements jitter (i.e., errors in georeferencing the scans) which in turn reduces the accuracy of wave profiling and wave prediction. Nonetheless, the complete reasons for the variation in the prediction accuracy in the field data observed in Fig. 4 remain a question for future work. In Fig. 5 we show box plots of the relative RMS error across the hour for time horizons $\mathcal{T}_1$, $\mathcal{T}_2$, $\mathcal{T}_3$, $\mathcal{T}_4$, and $\mathcal{T}_5$. Our first observation is that the error is within reasonable limits, and it is only higher during the dropout periods in the correlation observed in Fig. 4, i.e. there are no additional dropouts in the prediction quality.

Fig. 4 and 5 illustrate how the prediction accuracy deteriorates with increasing the prediction horizon. To further investigate the behaviour of the error in the predictable zones within the prediction horizons, we plot the second form of temporal correlation (11) in Fig. 6. The correlation (11) is evaluated at single time *instants* in the prediction horizons: 30 s, 60 s, 90 s, 120 s, and 150 s, across the trial duration over the corresponding predictable zone. We also plot the relative error $\varepsilon_s^p(z_m)$ in (15) versus the prediction time instants in Fig. 7.We can see in Fig. 6 that the correlation is rather poor beyond 120 s, which is not clearly observed in the correlation calculations shown in Fig. 4. It is clear from Fig. 6 and 7 that the prediction quality within the predictable zone monotonically decreases with the prediction time instant. With such simple relationship along with the Space-Time diagram, it will be a straightforward task for a DSWP intelligent system to determine the maximum available prediction horizon for given predictable zone and prediction reliability.

4.2 The vessel heave motion prediction

Most applications of DSWP will involve determining the predicted wave-induced motions of some floating body. In linear ship theory, vessels are typically modelled by 6 weakly-coupled ordinary linear differential equations that are typically Fourier transformed to produce a system of Frequency Response functions that are acted upon by the Fourier Transform of the wave system. Alternatively (and equivalently), the response of a narrow strip of vessel to an impulsive wave force input is integrated over the vessel hull profile (strip theory), giving rise to the so called response amplitude operators (RAO) coefficients. In either case, below resonance, the resulting heave Frequency Response function is crudely speaking a low pass filter. Consequently, at low wave frequencies relative to the ship's dynamics as prevail in the present situation (the resonance is at approximately a 9 s period with dominant wave systems centred on 11 s and 13 s), the heave transfer function is at least to a zeroth-order approximation constant. Similarly, the phase shift between wave forcing functions and vessel motion is again to a zeroth-order approximation zero. Hence, for heave motions, the vessel approximately follows the wave profile and to a first-order approximation there is no requirement to compensate for vessel motions. This is not the case in pitch where the response changes rapidly with frequency below resonance which is why only heave is considered here.

A high precision vessel motion sensor was present on the vessel. However, this was mounted 14 m forward and 2 m above the vessels nominal dynamic centre (as supplied by the vessel operators), with the vessel being 90 m in length. The sensor's location meant that other modes of motion made some contributions to the measured heave. Unfortunately the vessel had been "cut and extended" and in addition had considerable extraneous deck equipment all of which meant that the exact location of the motion centre was not well defined. This made it difficult to confidently decouple pure heave motion so the authors were forced to use the uncorrected motion senor data as a "raw heave" motion estimate. Thus, Fig. 8 shows the correlations between the wave predictions (taken to represent heave) and the raw measured vessel heave motion that was available to us in the time span 13:21 – 13:43 UTC, for prediction horizons $[\tau_s, \tau_s + 60]$ s and $[\tau_s, \tau_s + 120]$ s . Given the very crude nature of the heave assessment, the results shown are surprisingly good.

The drops in the prediction quality seen in Fig. 8 appear to correlate to some extent with changes in the vessel's heading and speed. Fortunately, the onset and the return to good prediction occur over a sufficiently long timescale for them to be recognised during operations. These drops are not present in the simulation work in Al-Ani et al. (2019) and as with the wave prediction estimates they would appear to be associated with the actual wave profile measurements of real seas rather than being fundamental artefacts of the prediction technique.

5. Conclusions

The level of errors encountered in the prediction based on the data obtained in the Golden Arrow sea trial indicates that in applications such as QPP (e.g., for operations such as launch and recovery of small craft and air vehicles), DSWP has real potential as a practical maritime tool. Drops occur in the prediction accuracy whose detailed cause remains a subject for further work. The absence of these in simulation studies indicates they are associated with aspects of the wave radar determination of actual sea profiles. However, from an application perspective, the onset of these occurs sufficiently slowly for them to be easily identified and thus not represent a barrier for future operations exploiting DSWP.

Acknowledgments

This work was supported by the EPSRC Research Grant EP/N009142/1. The authors wish to express their thanks to the UK Ministry of Defence for their support in collecting the data presented here.

References

Abusedra, L., and M. Belmont, 2011: Prediction diagrams for deterministic sea wave prediction and the introduction of the data extension prediction method. *Int. J. Shipbuild. Prog.*, **58**, 59–81.

Al-Ani, M., J. Christmas, M.R. Belmont, J Duncan, and B Ferrier, 2019: Deterministic Sea Waves Prediction Using Mixed Space-Time Wave Radar Data. *J. of Atmos. Oceanic Technol.*, in press.

Alford, L. K., R. F. Beck., J. T. Johnson, D. Lyzenga, O. Nwogu, and A. Zundel, 2015: A Real-Time System for Forecasting Extreme Waves and Vessel Motions. *Proc. of the 33rd Int. Conf. on Offshore Mechanics and Arctic Engineering (ASME).*

Bagchi, S. and S. K. Mitra, 1996: The nonuniform discrete Fourier transform and its applications in filter design. I. 1-D. *IEEE Trans. on Circuits and Systems II: Analog and Digital Signal Processing*, **43** (6), pp. 422-433.

Belmont, M., J. Christmas, J. Dannenberg, T. Hilmer, J.M. Duncan, J. Duncan, and B. Ferrier, 2014: An examination of the feasibility of linear deterministic sea wave prediction in multi-directional seas using wave profiling radar: theory, simulation and sea trials. *J. of Atmos. Oceanic Technol.*, **31** (7), 1601–1614.

——, J. Horwood, R. Thurley, and J. Baker, 2006: Filters for linear sea-wave prediction. *Ocean Eng.*, **33**, 2332–2351.

Bilinskis, I, 2007. Digital Alias-free Signal Processing. UK: John Wiley & Sons.

Blondel, E., G. Ducrozet, F. Bonnefoy, and P. Ferranti, 2008: Deterministic reconstruction and prediction of non-linear wave systems. *Proc. of the 23rd Int. Workshop Water Waves and Floating Bodies (IWWWFB)*, Jeju, Korea**,** 13–16.

Connell, B. H., J. P. Rudzinsky, C. S. Brundick, W.M. Milewski, J.G. Kusters, and G. Farquharson, 2015: Development of an Environmental and Ship Motion Forecasting System. *Proc. of the 34rd Int. Conf. on Offshore Mechanics and Arctic Engineering (ASME)*, Newfoundland, Canada, **11.**

Crossland, P., J.M. Duncan, and B. Ferrier, 2009: The feasibility of developing a quiescent period prediction system in a simulation environment. *Proc. of the Int. Conf. on Computer Applications in Shipbuilding (ICCAS)*, Shanghai, China, **2**. 751–762.

Edgar, D., J. Horwood, R. Thurley, and M. Belmont, 2000: The effects of parameters on the maximum prediction time possible in short term forecasting of the sea surface shape. *Int. Shipbuild. Prog.*, **47**, 287–301.

Ferrier, B., A. Baitis and A. Manning, 2000: Evolution of the landing period designator (LPD) for shipboard air operations. *Nav. Eng. J.*, **112** (4), 297–316.

——, J.M. Duncan, M. Belmont, A. Curnow and P. Crossland, 2013: Using simulation to justify and develop quiescent period prediction systems for the Royal Navy. *Proc. of the Int. Conf. on Computer Applications in Shipbuilding (ICCAS)*, Busan, South Korea, **2**, 99–107.

Giron-Sierra J. M. and S. Esteban S, 2010: The Problem of Quiescent Period prediction for Ships: A Review. *Proc. of the Int. Conf. on Control Applications in Marine Systems*. Rostock-Warnmünde, Germany, 307-311.

Hilmer, T., and E. Thornhill, 2014: Deterministic wave predictions from the WaMoS II, *Proc. of OCEANS'14*, Taipei, 1–8.

——, and ——, 2015: Observations of Predictive Skill for Real-Time Deterministic Sea Waves from the WaMoS II. *Proc. of OCEANS'15,* Washington, 1–7.

Kusters, J. G., K. L. Cockrell., B. H. Connell, J. P. Rudzinsky, and V. J. Vinciullo, 2016: FutureWaves™: A real-time Ship Motion Forecasting system employing advanced wave-sensing radar. *Proc. of OCEANS'16, Monterey*, 1-9.

Morris, E., H. Zienkiewicz, M. Pourzanjani, J. Flower, and M. Belmont, 1992: Techniques for sea-state prediction. *Proc. of the 2nd Int. Conf. on Manoeuvring and Control of Marine Craft*, Southampton, UK, 547–571.

Pourzanjani M., M. R. Belmont, H. Zienkiewicz, and M. Morris, 1992: Applications of a sea-surface estimator in predictive ship control. *Proc. of the 2nd. Int. Conf. on Manoeuvring and Control of Marine Craft*, Southampton, UK, 581–591.

Qi, Y., W. Xiao, and D.K. Yue, 2016: Phase-Resolved Wave Field Simulation Calibration of Sea Surface Reconstruction Using Noncoherent Marine Radar. *J. Atmos. Oceanic Technol.*, **33**, 1135–1149,

——, ——, Liu, Y., and Yue, D.K.P. 2018. Predicitable zone for phase –resolved reconstruction and forecast of irregular waves. *Wave Motion*, **77**, 195-213.

Reichert K., J. C. Nieto Borge, and J. Dittmer, 1999: Wamos II: A radar based wave and current monitoring system. *Proc. of the Int. Conf. on Ocean and Polar Engineering*, Brest, France, **3**, pp. 139–143.

Stoica, P., P. Babu and J. Li, 2011: New Method of Sparse Parameter Estimation in Separable Models and Its Use for Spectral Analysis of Irregularly Sampled Data. *IEEE Trans. on Signal Processing*, 59 (1), 35-47.

Taylor, K. E., 2001: Summarizing multiple aspects of model performance in a single diagram. *J. Geophys. Res.*, **106** (D7), 7183–7192.

Tucker, M. J., P. G. Challenor, and D. J. T. Carter, 1984: Numerical simulation of a random sea: A common error and its effect upon wave group statistics. *Appl. Ocean Res.*, **6**, 118–122.

Tucker, M. J., and E. Pitt, 2001: Waves in Ocean Engineering. Elsevier Ocean Engineering Series, 5, Elsevier.

Wijaya, A. P., P. Naaijen, and W. van Groesen, 2015: Reconstruction and future prediction of the sea surface from radar observations. *Ocean engineering*, **106**, 261-270.

Figure Caption List

Fig. 1 The standard deviation of the ship's heave over the trial period, as recorded by the Differential GPS sensor.

Fig. 2. The ship's heading, course and speed over the duration 12:58–14:00 UTC of the trial.

Fig. 3. The measurement zone in (a). The mean correlation coefficients in the corresponding predictable zone for prediction horizon $\mathcal{T}_1 = \left[\tau_s, \tau_s + 30\right]$ s in (b), $\mathcal{T}_2 = \left[\tau_s, \tau_s + 60\right]$ s in (c), $\mathcal{T}_3 = \left[\tau_s, \tau_s + 90\right]$ s in (d), $\mathcal{T}_4 = \left[\tau_s, \tau_s + 120\right]$ s in (e), and $\mathcal{T}_5 = \left[\tau_s, \tau_s + 150\right]$ s in (f).

Fig. 4. The correlation coefficients across the hour at the labelled time horizon in the corresponding predictable zone. Each box marks the upper and lower quartiles, with the centre being the median; the black dashed lines indicate the full range of values.

Fig. 5. The relative RMS prediction error across the hour at the labelled time horizon in the corresponding predictable zone. Each box marks the upper and lower quartiles, with the centre being the median; the black dashed lines indicate the full range of values.

Fig. 6. The correlation coefficients in the corresponding predictable zone for prediction time instant 30 s in (a), 60 s in (b), 90 s in (c), 120 s in (d), and 150 s in (e).

Fig. 7. The relative prediction error in the predictable zone versus the prediction time instants. Each box marks the upper and lower quartiles, with the centre being the median; the black dashed lines indicate the full range of values.

Fig. 8. The correlation coefficients between the WaMoS II based prediction and the "raw" vessel heave data.

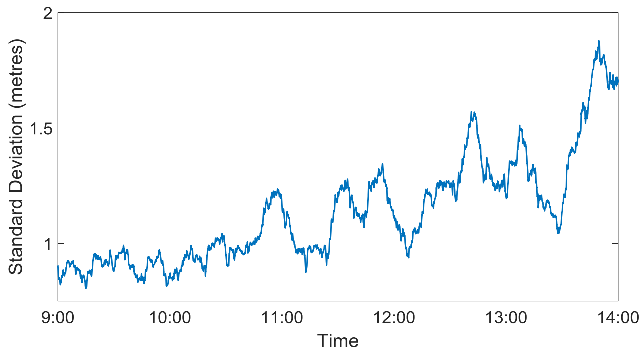

Fig. 1. The standard deviation of the ship's heave over the trial period, as recorded by the Differential GPS sensor.

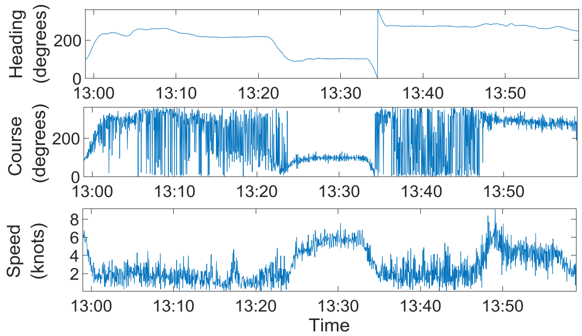

Fig. 2. The ship’s heading, course and speed over the duration 12:58–14:00 UTC of the trial.

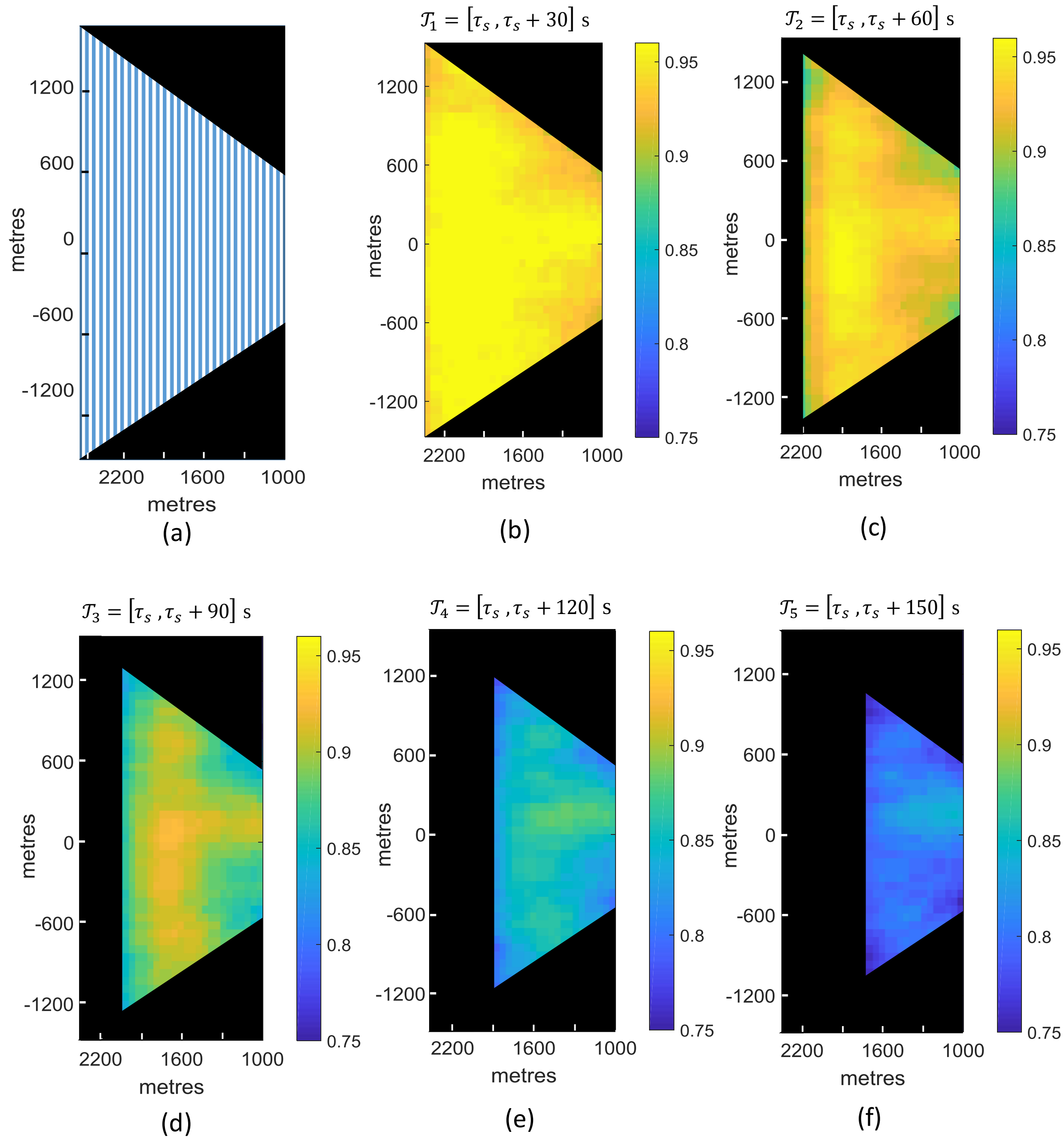

Fig. 3. The measurement zone in (a). The mean correlation coefficients in the corresponding predictable zone for prediction horizon $\mathcal{T}_1 = [\tau_s, \tau_s + 30]$ s in (b), $\mathcal{T}_2 = [\tau_s, \tau_s + 60]$ s in (c), $\mathcal{T}_3 = [\tau_s, \tau_s + 90]$ s in (d), $\mathcal{T}_4 = [\tau_s, \tau_s + 120]$ s in (e), and $\mathcal{T}_5 = [\tau_s, \tau_s + 150]$ s in (f).

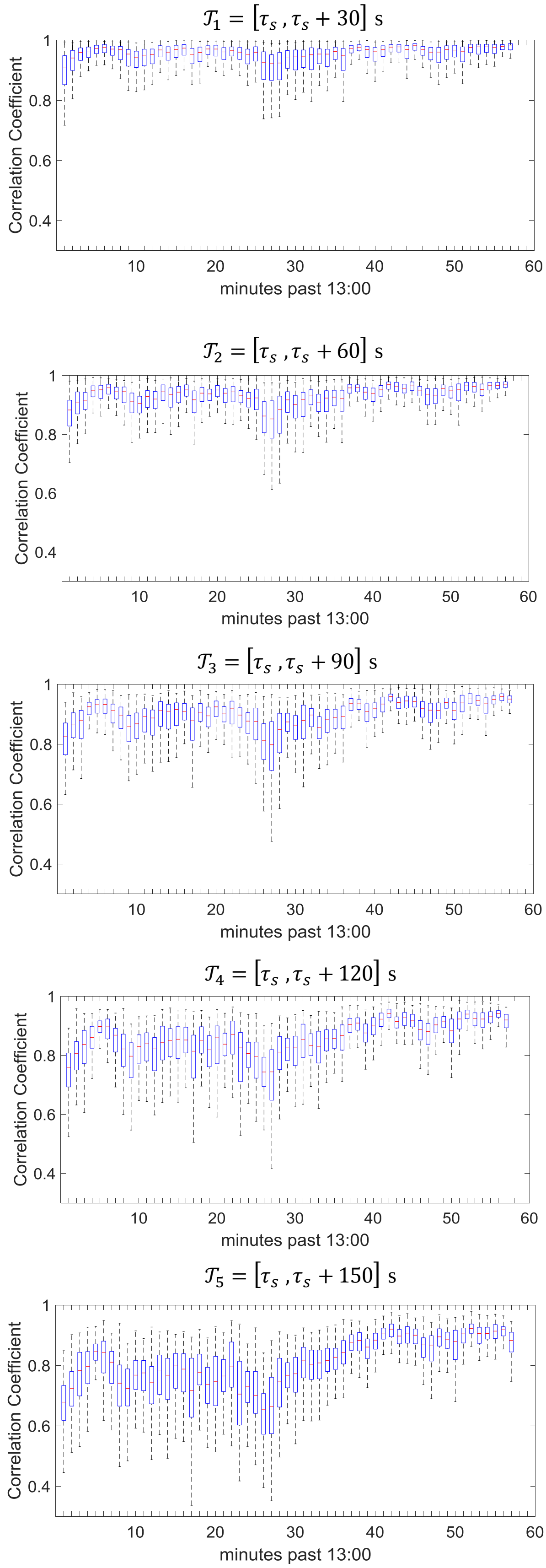

Fig. 4. The correlation coefficients at the labelled time horizon in the predictable zone. Each box marks the upper and lower quartiles, with the centre being the median; the dashed lines indicate the full range of values.

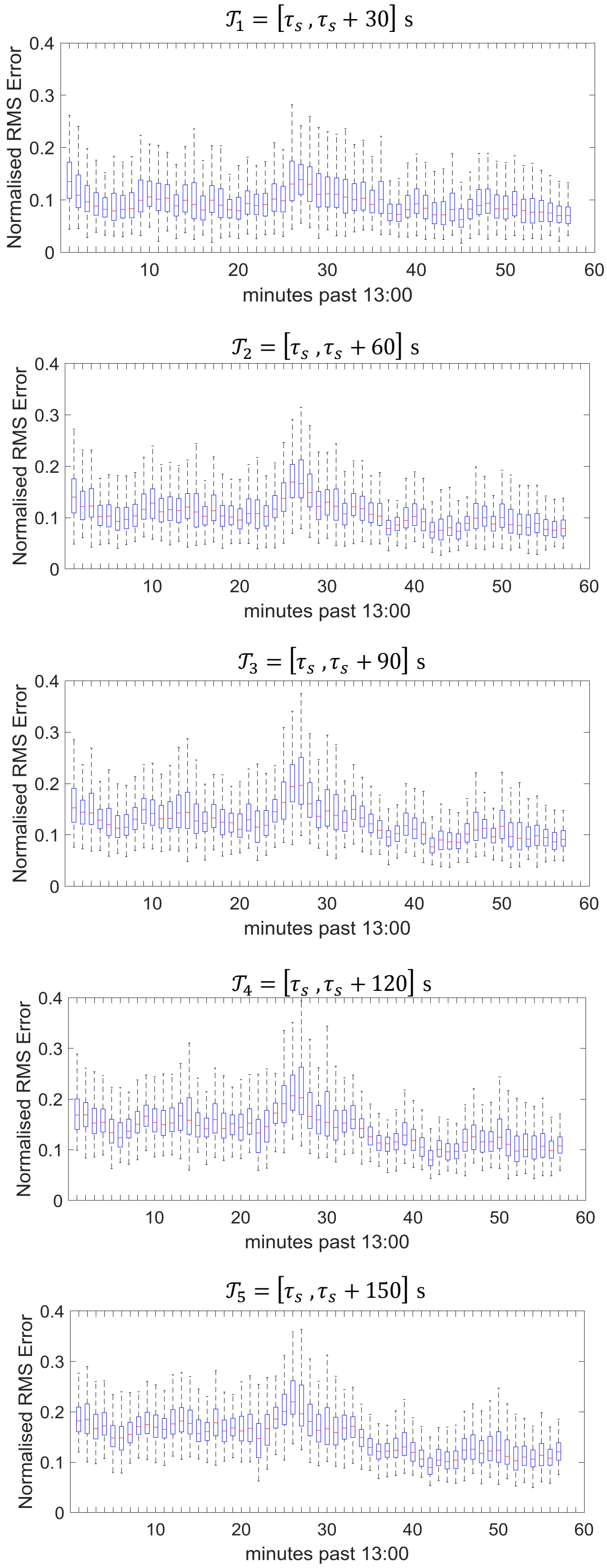

Fig. 5. The relative RMS prediction error across the hour at the labelled time horizon in the corresponding predictable zone. Each box marks the upper and lower quartiles, with the centre being the median; the black dashed lines indicate the full range of values.

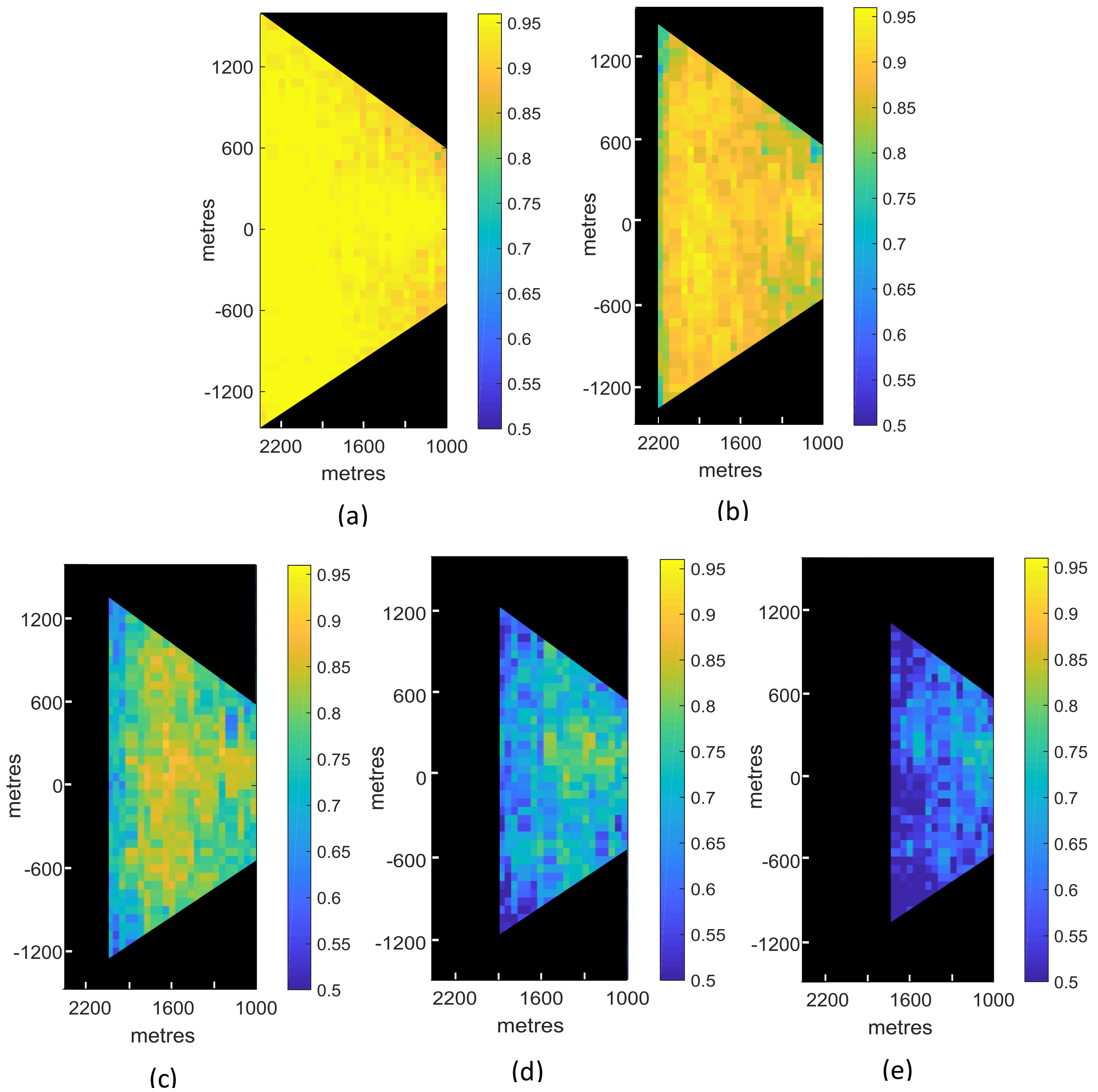

Fig. 6. The correlation coefficients in the corresponding predictable zone for prediction time instant 30 s in (a), 60 s in (b), 90 s in (c), 120 s in (d), and 150 s in (e).

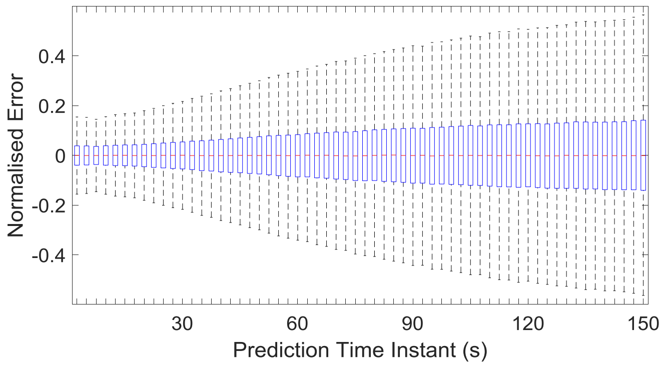

Fig. 6. The relative prediction error in the predictable zone versus the prediction time instants. Each box marks the upper and lower quartiles, with the centre being the median; the black dashed lines indicate the full range of values.

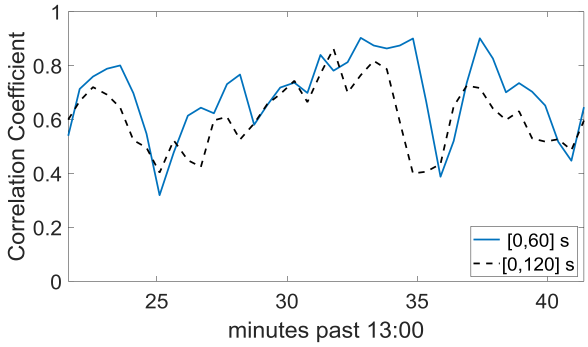

Fig. 7. The correlation coefficients between the WaMoS II based prediction and the “raw” vessel heave data.